Tiainen, Laura; Abreu, Pedro; Buciumeanu, Mihaela; Silva, Filipe; Gasik, Michael; Serna Guerrero, Rodrigo; Carvalho, Oscar

Novel laser surface texturing for improved primary stability of titanium implants

Published in:
Journal of the Mechanical Behavior of Biomedical Materials

DOI:
10.1016/j.jmbbm.2019.04.052

Published: 08/05/2019

Document Version
Peer-reviewed accepted author manuscript, also known as Final accepted manuscript or Post-print

Novel Laser Surface Texturing for Improved Primary Stability of Titanium Implants

Laura Tiainen[a,*], Pedro Abreu[a], Mihaela Buciumeanu[b], Filipe Silva[a], Michael Gasik[c], Rodrigo Serna Guerrero[c], Oscar Carvalho[a]

[a] *CMEMS-UMinho, University of Minho, Campus de Azurém, 4800-058 Guimarães, Portugal*
[b] *Faculty of Engineering, Dunărea de Jos University of Galaţi, 800008, Galati, Romania*
[c] *Department of Chemical and Metallurgical Engineering, School of Chemical Engineering, Aalto University, 00076, Espoo, Finland*

Abstract

Recently, the production of well-defined patterned surfaces with random or regular micro and nano-features has brought new opportunities for research and development in the field of tissue engineering and regenerative medicine. Among advanced micro and nano processing technologies, laser surface texturing (LST) stands out due to its simplicity, flexibility, precision, reproducibility and relatively low cost. This work studies the development of patterned surfaces controlled by of LST into biomedical grade V titanium, Ti−6 Al−4 V–alloy. We present different cross-hatched micropatterns followed by the characterisation of surface morphology and topography. Structural integrity of the produced patterns is evaluated by friction tests against bone, mimicking the insertion of an implant. Wettability is studied as it is crucial for protein adsorption and cell adhesion. The results show that the surface topography obtained using different patterning plans influences the wetting behaviour and the coefficient of friction against bone.

*Corresponding author Laura Tiainen
+351 927 552 529
laura.tiainen@me.com

Preprint submitted to Journal of the Mechanical Behavior of Biomedical Materials March 13, 2019

Keywords: Surface texturing, micropatterns, LST, Ti-6Al-4V alloy, dental implant material

---

A	Effective focal spot area	R_a	Arithmetic mean surface roughness
b	Distance between consecutive laser pulses	R_z	Average maximum peak to valley
		S_x	Laser spot overlap
E_{pulse}	Laser energy per pulse	ω	Radius of laser beam spot size
F_{eff}	Effective fluence	COF	Coefficient of friction
Q	Laser pulse total effective energy	$\theta^{'}$	Apparent contact angle

1. Introduction

Despite that in general the success and survival rates of dental implants are excellent, complications still occur and peri-implant diseases pose significant challenges for clinicians and patients. The primary stability, roughly the first two to four weeks after implantation, is defined by the mechanical stability on the traumatized bone, the bone healing process and possible infections. Biomechanical stability is completed by distant osteogenesis and contact osteogenesis at the implant surface. A clinical failure of an implant often implies the extraction of the dental fixture due to insufficient osseointegration (early failure) or bone maintenance (late failure) [1, 2]. The causes for early failures are related to poor bone condition, patient's health condition, lack of mechanical stability and infections among others [3, 2, 4, 5, 6]. Late failures are generally associated with functional overload, peri-implantitis and inadequate prosthetic construction [5, 7, 2]. Over the past thirty years, different approaches to alter implant surface characteristics have gained attraction in the bioengineering and biomedical field [8]. Surface modifications aim to increase control over tissue and cellular response through the modulation of the basic mechanisms of cell attachment, proliferation, differentiation and maturation [9, 10].

1.1. Implant surface

Several studies have demonstrated that by changing the implant surface, the rate of osseointegration and the percentage of bone-to-implant contact (BIC) can be significantly improved [11, 12, 13, 14]. Furthermore, is has been highlighted that the most relevant implant surface properties impacting the adhesion and the survival of cells are chemical composition, surface energy, wettability (hydrophobicity/ hydrophilicity), roughness, topography and surface morphology. Successful titanium alloys such as the Straumann SLA® and SLActive® and Biomet 3i T3®, have

good fatigue strength, adequate mechanical and physical properties (i.e. high specific strength, relatively low young modulus and low density) compared with other metallic biomaterials such as cobalt-chromium alloys and stainless steel [7, 8, 15]. The lower young modulus results in a more appropriative stress distribution at BIC [16, 17]. These titanium alloys also form spontaneously an adherent passive layer that inhibits corrosion in a physiological environment. In fact this oxide-rich layer is responsible for their excellent biocompatibility. [18, 19, 20, 7, 8]. Also, bioactive titanium can be prepared through anodic oxidation in H_2SO_4 solution, and these surfaces have been found suitable for loading-bearing applications [21].

Thus, it is well-known that additionally to the selected material, the surface topography at micro- and nanoscale has a direct impact on cell morphology, orientation, activity, behaviour and even on the phenotypic expression of various types of cells. Preliminary results indicate that there is substantial potential of reducing infection risks by 60-90%, without using any antibiotics, purely by optimising biomaterials to improve osteogenic cells proliferation by 15-30% [22, 23]. The different scales of dimension may have different roles in biomedical applications. It is suggested that the cellular fate and function can be modulated by both nano- and microscale cues as well as periodic structures [24, 25, 26].

The most employed features are grooves and ridges hence they have been widely investigated as well [27, 28, 29, 30, 31, 24]. In the majority of the cases, cells tend to align and spread along topographical discontinuities like the edges of grooves and ridges. The underlying biological phenomena of this contact guidance are yet to be uncovered but it is clear that there is a link to mechanotransduction. In a nutshell, cells can recognise topographies with heights ranging from a few nanometers to sev-

eral hundreds of micrometers. Different responses to similar surface topographies can be observed with large cells, such as osteoprogenitor cells (30∼50 µm), and small cells like monocytes (∼10 mm), platelets (∼2 µm) or even bacteria (∼1 µm) [32, 33, 34].

Cell adhesion is preceded by the adhesion of ions and proteins on the surface. Hydrophilic surfaces promote higher degree of protein adsorption when compared with the hydrophobic counterparts [35]. Also initial attachment of osteoblastic cells increases with increasing hydrophilicity [36]. However, moderate hydrophilicity ($\sim 40^\circ < \theta_{H_2O} < \sim 70^\circ$) is more advantageous by promoting balanced protein adsorption and better initial interaction, motility, proliferation and differentiation of cells [37, 38, 36, 35].

Producing well defined regular micropatterns is difficult by sandblasting and chemical machining as sandblasting is by nature a chaotic process. Etching on the other hand suffers from the impressive corrosion resistance of titanium alloys and the formed passive oxide layer furthermore, the processes often rely on hazardous chemicals [39]. Establishing the cause–effect relationships between specific features and promotion of faster, long-lasting osseointegration requires well defined features. Laser surface texturing (LST) allows development of novel surfaces for this purpose.

1.2. Laser surface texturing

Laser surface modification techniques make use of the thermal and photonic effects associated with the interaction of the laser beam with various engineering materials [40]. The ejection of material from the target surface is characterised by absorption of a massive quantity of energy. The mechanism of removal is based on ablation or vaporisation. In most cases, thermal conduction and fluid dynamics effects can

also be observed [40]. Depending on the power density and temporal working mode of the laser, specific ablation mechanisms can prevail over others [41]. Evidently, material processing by laser is dependent on a large number of process variables that influence directly the laser–material interaction and ultimately the processing efficiency and quality. Thus, the topography and chemistry of the surfaces can be optimised for the desired biomedical application.

2. Materials & Methods

Laser surface texturing method was employed to produce various micropatterned surfaces on biomedical grade V titanium alloy, Ti−6 Al−4 V to enhance vascularisation and bone adhesion. Cross-hatch patterns were selected in order to increase the effective surface area for bone–implant contact. Research on the hierarchical structures of bone and behaviour of osteoblastic cells has shown that cross-hatch patterns hold a higher adhesion work when compared against micro-dimples or chaotic surfaces produced by direct laser texturing [31]. Wettability and friction tests were performed to characterise and compare the different patterns against two control sample types; grit-blasted and polished biomedical grade V titanium. At least three samples of each pattern were processed.

2.1. Sample preparation

The specimens were cut from two rods with diameters 6 mm and 24 mm, polished with silicon carbide (SiC) papers and cleaned. The final thickness of the samples was 2 mm ± 0.02 mm. Removing the particles produced in the polishing is essential as they induce defects upon the laser treatment. To obtain the high reproducibility of the micropatterns, the samples were ultrasonically cleaned for 5 min first in a detergent solution and then in acetone or isopropanol. The samples were then rinsed

thoroughly with distilled water and left to dry in a desiccator overnight at room temperature.

The layout of different patterns, division into groups and the structural nomenclature used, are presented in Fig.1. The ridge and groove widths were designed to have uniform dimensions. A total of nine combinations with varying groove width (40 µm, 80 µm, 140 µm) and groove spacing (0 µm, 20 µm, 100 µm) were defined. The designs were drawn in SVG format using the freeware graphic editor software Inkscape (v0.91). The patterns were placed in three groups according to the spacing between consecutive grooves.

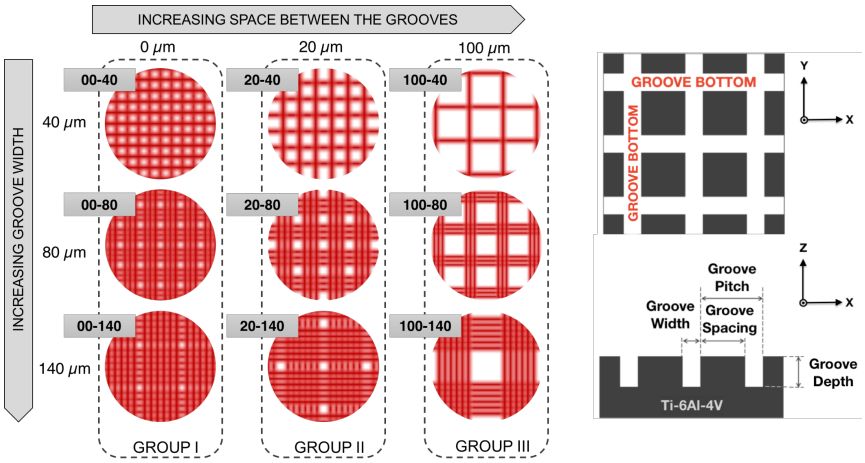

Figure 1: A schematic illustration of the patterns (not to scale) as well as the nomenclature and grouping used for the combinations. Lasered grooves are marked in red and untouched areas in white (left). Top and side view respectively (right)

LST presented in this work was performed using a Q-switched diode-pumped Nd:YAG laser (OEM plus 6 W, SISMA, Italy). The laser specifications are tabulated

in Table 1. The system is equipped with a galvanometer scanning head (2-axis sub-system Focus shifter, model MS-10 [Y] D1 V2, from RAYLASE) and a 160 mm f-theta objective for focusing the beam and rastering the patterns. The input aperture of the laser beam is 10 µm. Pulsed lasers are usually characterised by beam shape, beam quality M^2, spot size (d_0), peak power (P) and fluence (F, laser energy E, delivered per effective focal spot area A). Laser beam has circular Gaussian shape profile (TEM00) and the theoretical focal spot size (d_0) calculated in accordance with ISO Standard 11146 is 39 µm [42]. Moreover, the spot size depends greatly on the focusing of beam.

Table 1: Technical specification of SISMA OEM plus 6W

Laser Specifications	
Average Output Power [W]	6
Wavelength [nm]	1064
Laser Technology	Nb
Repetition Rate [kHz]	20
Pulse Width [ns]	35
Maximum Pulse Energy [mJ]	0.3
Beam Quality Factor, $M^2 <$	1.8
Cooling System	Forced-aired Cooling
Power Supply	230 V, ±10 %,, 50/60 kHz

Fluence is a position-dependent value and meaningful only in combination with irradiation time. Assuming a uniform temporal and spatial beam distribution, total effective energy (Q) per unit are gives the effective incident laser fluence (F_{eff}) that can be calculated using the following equation.

$$F_{eff} = \frac{Q}{A} \tag{1}$$

As the pulsed laser beam moves with a constant scanning speed. The the spot

overlap (S_x) between consecutive pulses is related to linear scan speed which is illustrated in Figure 2.

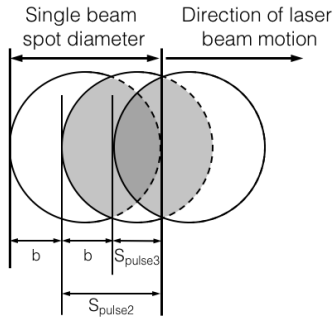

Figure 2: Overlap of successive laser pulses over a single spot area.

Thus, the contribution of each pulse to total effective energy (Q) delivered in a single spot area can be described as sum over the number of the pulses. In Eq. 2, E_{pulse} is the laser energy per pulse. The beam diameter (2ω) at the focal plane defined by [42] is twice the distance between the maximum peak intensity of the beam and the point where the beam energy in no more than $1/e^2$ ($\sim 13.5\,\%$) of the maximum intensity.

$$Q = \sum_{n=1}^{N} \left[\frac{2\omega - (1-n)b}{2\omega} \right] E_{pulse} \tag{2}$$

In the comparison of different laser operation settings, this contribution of pulses over a single spot area was taken into account by using the effective fluence F_{eff} (Eq.1).

All samples were textured in room air and assisted with a jet of air to remove debris produced during processing. The patterns that have groove width larger than the spot size were produced by overlapping multiple scan lines with an offset of half

the spot size until the desired width was reached. This methodology was adopted in an attempt to produce regular and flat-bottom microgrooves, since changing the wobble amplitude only resulted in highly irregular V-shaped grooves. The effective laser fluence was $7.47\,\mathrm{J/cm^2}$ per a scan line. The laser parameters used were average power 1.2 W, scan speed 400 mm/s and 10 laser passes per line. The grit-blasted control samples were P4000 grit polished 6 mm Ø Ti−6 Al−4 V disks, grit-blasted 30 s with alumina particles of 149 µm average size.

2.2. Wettability tests

Wetting is most often characterised by the contact angle between the material and water, WCA. The apparent contact angles θ' of patterned Ti-alloys and polished alloy were studied. The samples were cleaned the previous afternoon using the procedure described earlier and left to dry in a desiccator overnight. Measurements were taken with an optical tensiometer (OCA 15 plus, Dataphysics, Germany) using 5 µL of freshly made type I ultrapure water (18.2 MΩ cm, ELGA PURELAB® Classic) and 10 µl analytical grade glycerol (PA Hi-media, purity > 99.5 %, JMGS). The dispensing rate was $5\,\mu\mathrm{l\,s^{-1}}$. Room temperature during all the measurements was ∼20 °C. The determination of apparent contact angels was done with DataPhysics SCA -software using the Laplace–Young's method, after fitting drop outline to the recorded images. The substrate baseline was set manually and tilting was disabled.

The micropatterned samples are evidently far from an ideal polished surface and the liquid may spread throughout the pattern (Wenzel wetting theory) on the top of the features (Cassie–Baxter wetting theory) or by mixing the two mechanisms. The dimensions of the textures presented here are slightly large and obtaining Cassie–Baxter behaviour in 140 µm groove is unlikely. However, the features of the patterns

are not smooth and entrapment of air is possible. Moreover, the obtained apparent contact angles can be reasonably used as a comparative parameter of hydrophilicity. Surface energies are not evaluated as the textures may introduce capillary effect and bias through chemical heterogeneities and topography.

2.3. Friction tests

The parallelepipeds of bone had been extracted from the femoral part of an indigenous breed 8-month-old bovine, machined into rectangular ($4x16x20$mm) samples. During this preparation the bone was continuously moistened with PBS solution. For storing the samples were immersed in PBS and frozen. The bone hardness 125.2 HV$\pm$4.9 was obtained by load controlled micro indentation. The initial load was 0.8 mN, maximum load 3 N, rate 12 mN s^{-1} and the dwell period at maximum load 15 s.

The entire surface of Ø 6 mm disks was patterned for these tests. Prior to friction tests, the disks were cleaned sequentially in acetone, isopropanol and distilled water for 5 min and then left to dry in a desiccator overnight at room temperature. At least three samples of each micropattern were tested using a new bone plate for every new test. In addition, the coefficients of friction (COF) of alumina grit-blasted Ti$-$6 Al$-$4 V samples was measured for comparison. Hardness of the patterned surfaces was not studied. Grade V titanium hardness is roughly 347.0 HV.

The friction experiments were performed on a reciprocating pin-on-plate tribometer (Bruker-UMT-2, USA). An illustration of the friction tests performed in this work and a schematic coefficient of friction (COF) curves are shown in Fig.3. The defrosted bone plates were mounted in an acrylic electrochemical cell attached to the

tribometer and lubricated with standard PBS. A 50 N load was applied at 1 Hz frequency and 3 mm amplitude at 37 °C. The initial static coefficient of friction (COF) is determined by a single displacement in one direction. The measurement of the dynamic coefficient of friction follows immediately. The cycles of reciprocating slidings take 15 s after which the final static coefficient of friction is determined in a single displacement in the opposite direction of the initial COF. Total duration of the three tests was 25 s.

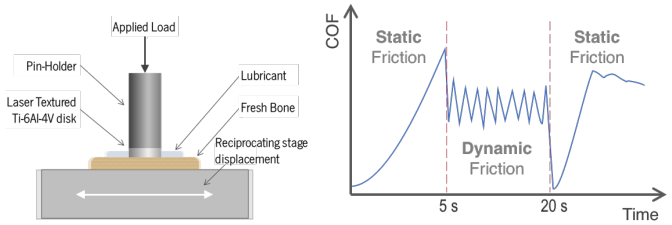

Figure 3: Bruker-UMT-2 tribometer or could be left out. A schematic representation of the friction test. Initial, dynamic and final static friction are measured in one measurement cycle of 25 s.

2.4. Characterisation methods

The laser-textured surfaces were characterised in terms of topography, morphology, chemical composition and surface roughness. All samples were inspected by naked eye and an optical microscope (Hund H500, Helmut Hund GmbH, Germany; or Leica DM 2500M, Leica Microsystems, Germany) for defects. The surface topography, morphology and surface chemical composition were characterised with an ultra-high-resolution field-emission Scanning Electron Microscope (NanoSEM - FEI Nova 200 (FEG/SEM) with integrated EDAX - Pegasus X4M (EDS/EBSD)) with a built-in Electron Backscatter Diffraction (EBSD) detector and microanalysis X-ray system (EDS). Surface topography was observed in both Secondary Electron (SE) and Back Scattered Electron (BSE) modes. Micrographs were acquired at low and high mag-

nifications in order to visualise the morphology at different scales. In addition, elemental surface analysis was performed by EDS which is suitable for microscale bulk composition analysis. The information gathered in SE and BSE modes is different and for instance dimensions measured in BSE mode with high magnification were ∼20 nm larger than in SE mode. Thereby, SEM imaging presented here is primarily secondary electron imaging since the main concern was the topographic contrast. Backscattered electrons have chemical contrast that is useful for inspection after the friction tests.

Oxidation in the patterns was studied with X-Ray diffraction (Bruker D8 Discover) at SEMAT, Guimaraes. Confocal Raman microscope (WITec Alpha300M+, Witec Ulm Germany / Izasa Portugal) and XPS (Thermo Scientific Escalab 250 Xi) measurements were taken the INL, Braga. However, both XRD and confonical Raman were not suitable for the purpose. Lastly, surface roughness was measured using a mechanical profilometer (Surftest SJ 201, Mitutoyo, Tokyo, Japan). Contact surface roughness was measured in accordance to ISO 4288:1996 standard [43, 44]. The profilometer was equipped with Ø2 µm and 70° opening angle diamond stylus. The sampling length was 1.5 mm for every new measurement. The measurement was repeated at least five times on different regions parallel to the scanning direction.

3. Results

The following subsections describe the morphology of each group of patterns in detail. The groove width affected the wettability of the surfaces more than the characteristic feature. A switch from hydrophobicity to hydrophilicity was observed in all groups and the results with glycerol follow the same trend. It seems that narrow grooves induce hydrophobicity and wider groove width hydrophilicity. The

improvement in the friction performance is evident when comparing all the cross-hatched surfaces with the grit-blasted ones. The dynamic coefficient of friction is higher by a tenth and the static friction at the end of the measurement shows a behaviour different from the grit-blasted control.

3.1. Microstructural characterisation

A general trend in the influence of laser texturing design on the micropatterns, is that the increase in number of intersections produces a lower relief of features. The groove aspect ratio decreased with the increasing groove width in all groups. During processing localised heat build-up induces a heat affected zone around the treated area which promotes oxidation and microstructural changes near the surface [45, 46, 47, 48, 49]. In the case of several laser passes, recasted layers are formed. Depending on operation parameters different titanium oxides, could be formed [46, 50, 51]. Due to the small volume fraction of local superficial oxidation in our patterns, the oxides species were beyond detection. Contribution from mainly the metal alloy precluded the collection of Raman spectra. Hence a more surface sensitive method, XPS, was used to take measurements on three different patterns (00-40, 20-80 and 100-80) and a polished reference sample. High heating rates of the substrate can also be associated with formation of microcracks and fatigue. Some microcracks were found particularly in the combinations with higher groove spacing and wider grooves. The 100–140 µm combination was observed with some fracturing of the sidewalls. In all groups the groove bottoms in combinations XX–80 and XX–140 have wavy roughness perpendicular to the texturing direction that is most visible in this group in Fig.4c.

3.1.1. Group I – Spikes, No spacing between the grooves

Beginning with the results from Group I in Fig.4, the characteristic features within this group are spikes and pits arranged in a very orderly fashion relief is very

narrow and accentuated. The SEM images below present a top, cross-section and 40° tilted view of the pattern. Increase in the groove width decreases the number of peaks per unit area and gives the pattern a square shape. Concurrently, the relief becomes less pronounced and porosity starts to occur. The spikes in these patterns are located on the edges of intersections and in the case of the largest 140 µm groove width (see Fig.4c) the valleys between the edges are relatively flat.

3.1.2. Group II –Towers, 20 µm *spacing between the grooves*

The topographical and morphological differences between the combinations in this group are evident. The pattern with smallest, 40 µm, groove width (Fig.5a) has a well-defined arrangement of tower-like structures Applying larger widths 80 and 140 µm (Fig.5b and Fig.5c) resulted in patchy towers with round and pointy edges. It is also noteworthy, that these towers seem to be partially hollow inside. It is likely that the recasting of layers form the cavity. In addition, the two patterns with larger groove width have porosity but it is not extravagant.

3.1.3. Group III – Untreated square islands and rises sidewalls

In this final group all the combinations have untreated square islands (∼100 x 100 µm) surrounded by raised sidewalls of resolidified material. The common trend of change from U-shaped grooves to rectangular grooves with considerable degree of roughness was observed here as well Fig.6. As expected, the aspect ratio of the grooves (depth/width) decreased with increasing groove width from 0.77 to 0.11. Porosity was found sparsely only on the widest groove combination. 6c.

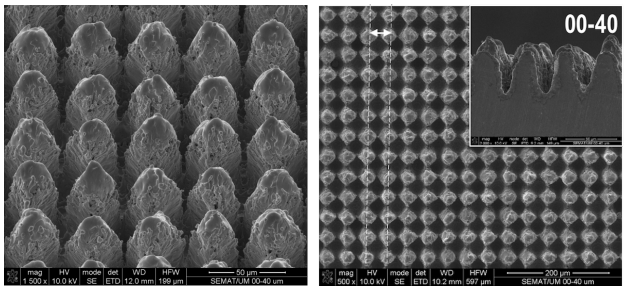

(a) Pattern 00–40. Groove width 40 µm

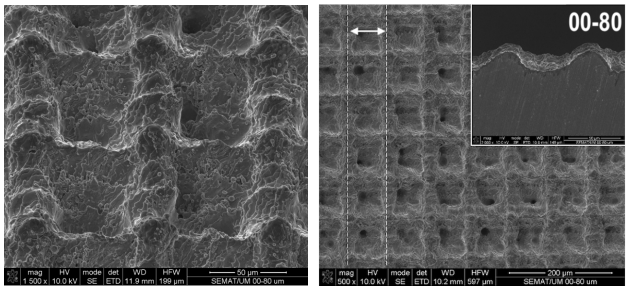

(b) Pattern 00–80. Groove width 80 µm

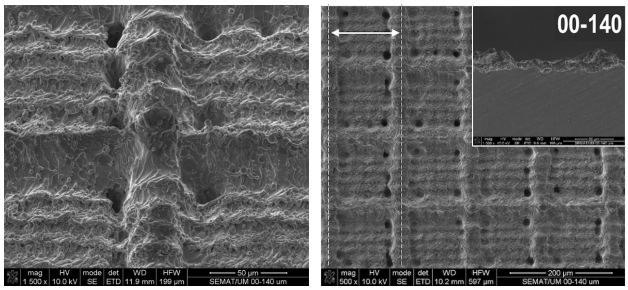

(c) Pattern 00–140. Groove width 140 µm

Figure 4: SEM images of micropatterns from Group I. Characteristic features in this group are spikes and pits. No spacing between the grooves. The groove width is measured as the white arrows indicate on the top view (left). Magnification at 40° tilt (left).

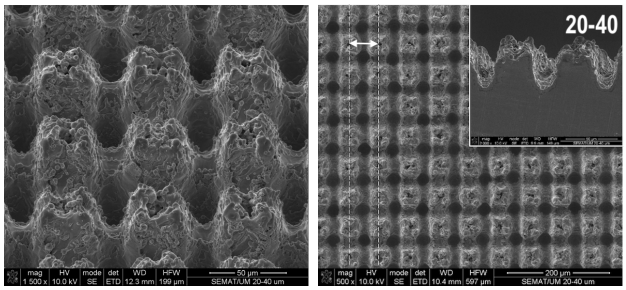

(a) Pattern 20–40. Groove width 40 µm

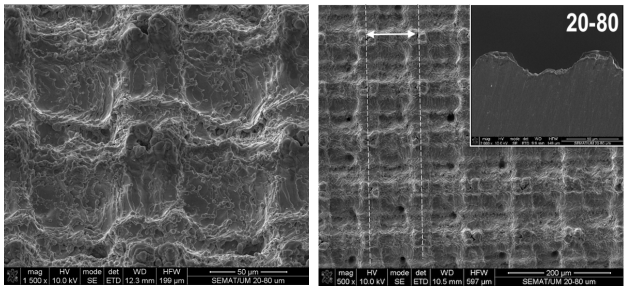

(b) Pattern 20–80. Groove width 80 µm

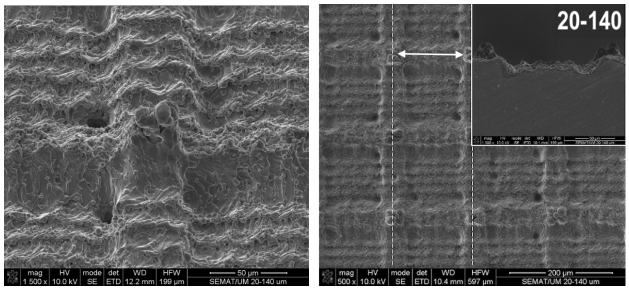

(c) Pattern 20–140. Groove width 140 µm

Figure 5: SEM images of micropatterns from Group II. Characteristic features in this group are tower-like. 20 µm spacing between the grooves. The groove width shown by white arrows. Magnification at 40° tilt (left).

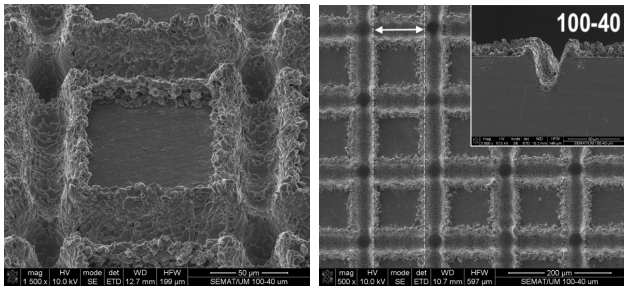

(a) Pattern 100–40. Groove width 40 µm

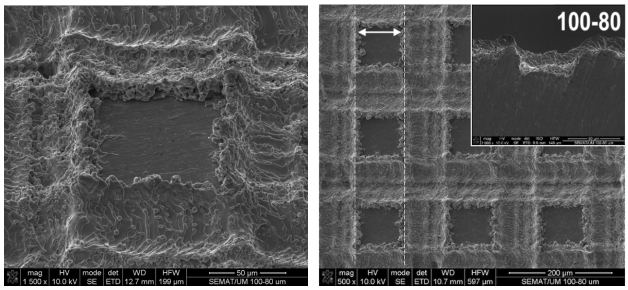

(b) Pattern 100–80. Groove width 80 µm

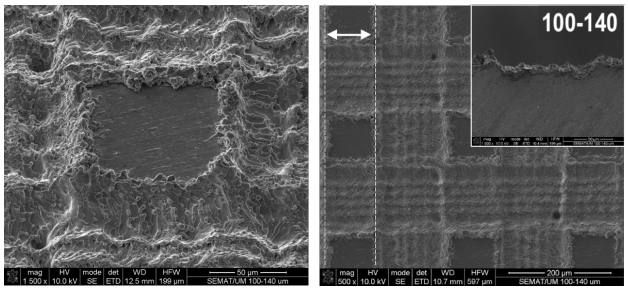

(c) Pattern 100–140. Groove width 140 µm

Figure 6: SEM images of Group III micropatterns. Untreated square islands surrounded by raised sidewalls. 100 µm spacing between the grooves. The groove width shown by white arrows (left). Magnification at 40° tilt (left).

To summarize, it is evident that the design of both the grooves and the processing reflects in the structural integrity of micropatterns. Particularly, the textures with wider grooves exhibit more microcracking and porosity. Grooves with 40 µm were composed of one marking scan line, whereas grooves with 80 µm and 140 µm needed respectively three and six parallel marking lines. Since the wide grooves are composed by multiple overlapping scan lines, the recast layers from the first marking lines might have "neighbouring" thermal effects and higher oxidation. When the adjacent scan lines induce changes in the previous heat affected zones, also mismatches between the microstructural phases and the superposed recast layers increases and microcracks will eventually appear [48, 47, 52].

The groove width, spacing and depth were measured from the SEM images by image analysis with ImageJ software. The data extracted from cross-sectional SEM images (see Fig.4, 5 and 6) is presented in Table 2. The groove width and spacing were close to the set point values. A peculiar deviation is observed within Group II where the groove width is 10 µm less and the groove spacing 10 µm more than the target value. This may be explained by processing inaccuracy occurred during laser texturing, pattern drawing or laser focusing for example. Regarding the depth of the grooves, increasing the groove width results in smaller depth. The deepest grooves are found in Group I and the lowest are obtained in Group III. This is explained by the material accumulation from previous laser passages onto the adjacent ablating tracks (marking lines) and by deviations in energy density.

The arithmetic mean surface roughness (R_a) and average maximum peak-to-valley (R_z) calculated from the surface profiles are also presented in Table 2. The

Table 2: Dimensions of the patterns. The mean ± SD [µm] from image analysis of cross-sectional SEM images. Arithmetic mean (Ra) and average maximum peak-to-valley ratio (Rz) in accordance to ISO 4288:1996.

Pattern combination		Groove spacing	Groove width	Depth	depth/width	Ra	Rz
Group I	00–40		39.5 ± 0.5	49.0 ± 3.1	0.19	6.3 ± 0.4	33.4 ± 2.6
	00–80		81.1 ± 1.7	21.5 ± 1.6	0.27	6.1 ± 1.1	23.5 ± 3.2
	00–140		137.1 ± 2.5	26.4 ± 1.3	1.24	4.5 ± 0.3	23.4 ± 1.2
Group II	20–40	32.7 ± 2.4	28.9 ± 1.9	46.0 ± 4.3	0.17	6.1 ± 1.2	26.6 ± 4.0
	20–80	30.5 ± 2.9	68.0 ± 2.5	20.2 ± 1.9	0.30	6.8 ± 0.5	24.6 ± 2.0
	20–140	35.4 ± 4.9	123.5 ± 4.4	21.3 ± 2.3	1.59	4.2 ± 0.7	21.5 ± 2.9
Group III	100–40	69.9 ± 1.5	42.1 ± 1.5	32.3 ± 1.7	0.11	4.9 ± 0.6	27.4 ± 1.8
	100–80	99.8 ± 4.1	77.0 ± 3.5	20.8 ± 2.0	0.27	4.0 ± 0.4	20.9 ± 1.8
	100–140	101.6 ± 3.9	136.5 ± 2.7	15.2 ± 3.3	0.77	3.1 ± 0.5	18.8 ± 2.8
Grit-Blasted						1.9 ± 0.1	14.5 ± 0.5
Polished						0.25 ± 0.03	1.8 ± 0.2

obtained average mean roughness R_a of the polished samples was ∼0.25 µm and the grid-blasted samples' $R_a \sim 2$ µm. The average roughness values were higher on the combinations with lower spacing and narrower grooves. Within the groups increasing groove width decreases the average roughness, except in the group II. The average maximum peak-to-valley describes the surfaces more consistently and the groove depth is in accordance with values obtained with SEM. Unlike the roughness of grit-blasted and polished surface, the values from the cross-hatched patterns ought to be prudently treated, since their topography is uneven, *i.e.*, the roughness on the grooves is different from the roughness of the plateaus. Therefore 2D profiles presented in Fig. 7 are more informative for representing differences between the patterns.

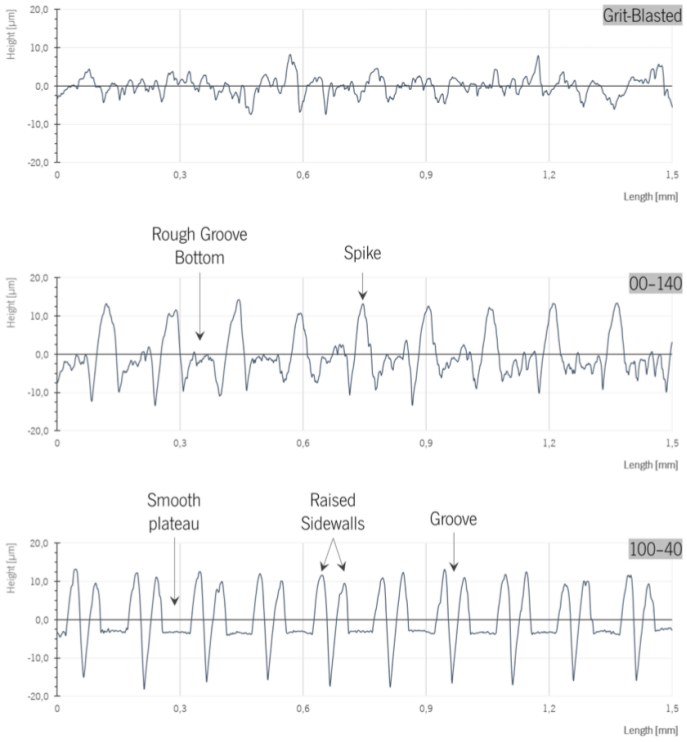

Figure 7: 2D roughness profiles of Grit-blasted surface (top) and two cross-hatched patterns 0 – 140 µm (middle) and 100 – 40 µm (bottom). The profile is a convolution of the surface and the diamond stylus.

Interestingly, all the micropatterns had nanostructures in the areas where the laser had passed. These features were not highly perceptible on SEM, but there seems to be a net-like-structure of very thin filaments. Figure 8 below shows how this anomalous net is superimposed onto the microstructures at both groove edges and bottom. Although these nanofeatures are a very exciting standpoint for applications, they peal off easily during cleaning (see Fig.8e).

3.1.4. Chemical analysis

Analysis on the chemical composition here are limited to elemental composition. Surface analysis by XPS describes the composition of metals and their oxides. EDS

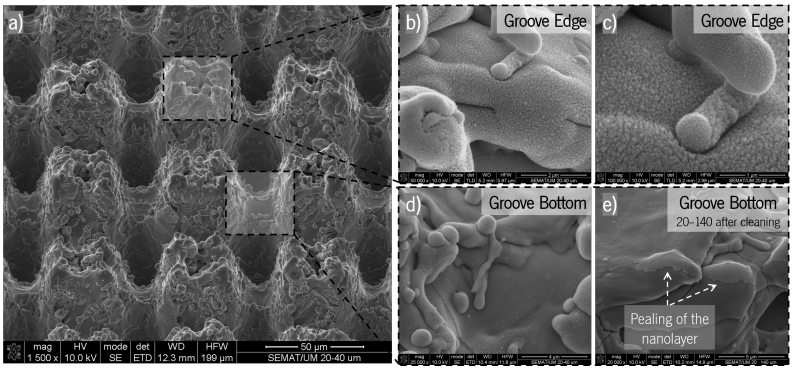

Figure 8: SEM images from combination 20–40 µm (a, b, c and d) showing the nanostructures superimposed onto the microstructures created by thermal ablation, on both groove edge (b, c) and bottom (d). The bottom right corner (e) corresponds to groove bottom from combination 20–140 µm after cleaning.

is micro scale bulk analysis. Techniques available to evaluate polymorphs, XRD and Raman spectroscopy, did not have the sensitivity needed.

From the EDS analysis (Fig.9, Tab.3), it can be concluded that there are different degrees of contamination and perhaps oxidation in different locations of the micropatterns. Proportions of other elements did not changed significantly. Figure 9 shows a representative case of Group III sample where chemical analysis is carried out on three areas with different exposure to laser treatment. As the material ablation is greater on the central area of the laser beam this likely contributed to the EDS results in Table 3. The formed oxide layer from first laser pass may have been partially removed due to the action of the second pass [47]. As observed, the higher atomic content of carbon in the area with material pile-up might indicate higher susceptibility to surface contamination on these areas. Even though EDS is a poor method for the evaluation of oxygen content, the difference in oxygen count from non-treated and lasered areas is significant, yet, this comparison should not be

made between the two laser treated areas, A2 and A3.

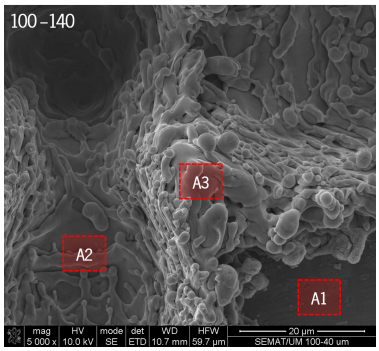

Figure 9: SEM/SE image of 100–40 on the corner of a square island. EDS taken at locations A1, A2 and A3. Recasted layers on the edges and sidewall.

Table 3: Elemental content (at.%) at A1, A2 and A3 in Fig. 9. Simulated spatial resolution of EDS is ∼1.8 µm.

	Non-treated A1	Laser-treated A2	Laser-treated A3
Ti	75.63	43.46	34.79
Al	11.65	6.03	4.91
V	2.74	1.57	1.11
O	2.34	41.90	48.78
C	7.64	7.05	10.40
O / Ti	0.03	0.96	1.40

The XPS results in Table 4 show that the surface was only partially oxidized in all inspected patterns. The curve fitting and experimental are available in appendix. Samples were cleaned with Ar clusters (6 keV 1000 Ar atoms per cluster). Highest oxidation in at% was found on the polished surface but all patterns have more TiO_2 and less TiO_X than the reference. However, the ratio of TiO_2 / TiO_X changes upon processing. The pattern with most processed surface area, 00-40, had most TiO_2 with respect to TiO_X. Counter intuitively, the 00-40 pattern has also most metallic titanium and the Group III texture with non-processed islands was oxidised the most upon laser processing.

In comparison to the reference, the surface composition of other constituents in the alloy changed as well. Fraction of metallic aluminium increased with patterning being highest in 00-40. Aluminium oxides with respect to polished substrate, were found less on the spiky 00-40 surface and contradictory slightly more on 20-80 and

100-80 patterns. Vanadium oxides had no large variations except increase in 100-80. In the tower-like and spiky samples the metallic vanadium dwindled. Overall these specimens from Groups II and III were most alike. In 100-80 the higher percentage of aluminium oxide and vanadium in it's metallic and oxide form, may be due to diffusion from the bulk for example. The spiky 00-40 surface stands out with composition differing most from the polished. Some shadowing effects may have take place and the tips of pattern may be over-represented in the data.

Table 4: XPS Results on titanium oxidation and composition in at% for Ti, Al and V and their oxides.

	Ti met	TiO_x	TiO_2	Al met	AlO_x	V met	VO_x	TiO_2 / TiO_x
Polished	1.52	11.39	16.9	0.43	4.69	0.13	0.19	1.48
00-40 Group I	2	2.95	18.02	1.52	2.4	0.07	0.22	6.11
20-80 Group II	0.83	4.61	18.03	0.64	5.27	0.05	0.2	3.91
100-80 Group III	0.63	7.97	18.52	0.64	5.38	0.12	0.34	2.32

3.2. Surface wettability

The results obtained from sessile drop measurements with ultrapure water and glycerol are presented in Fig.10. Glycerol was used to study the interaction of a less polar and more viscous liquid. The textured surfaces showed slightly better wetting with glycerol whereas the smooth control surface had the opposite tendency.

In all the groups, it is possible to observe a switch from poorly wettability to moderate wettability with increasing groove width. The wider grooves induce rough and chemically heterogenous area by more laser passages and adjacent tracks. In

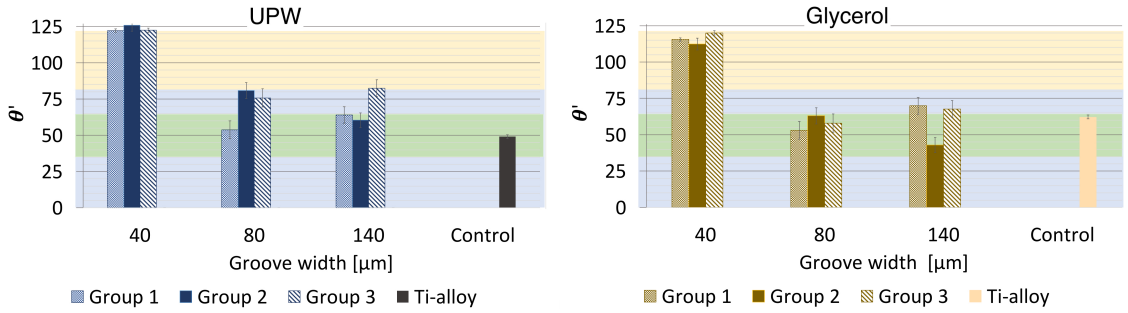

Figure 10: Average apparent contact angles obtained by sessile drop measurements 30 days after fabrication. Hydrophobic regime in ($\theta' > 90°$, yellow), hydrophilic regime ($\theta' < 90°$, blue) and moderate hydrophilicity (green).

fact, increasing the groove width from 40 to 80 µm, resulted in transition towards the hydrophilic regime. As seen from the comparison between Groups with similar groove widths, it seems clear that the groove spacing affected wettability within experimental error. The characteristic features of the combinations with smallest grooves width, xx–40 µm have deeper valleys and pointy well-defined spikes, towers and sidewalls that may cause entrapment of air and pinning of the drop edge. When comparing the results from the micropatterns with larger grooves, 80 µm and 140 µm, the variation in θ' is not so pronounced. Indeed, small deviations are observed and the apparent contact angle values of both liquids are similar to the smooth control surface results. The contact line between the sample and liquid is different on different patterns.

All things considered the comparison of wetting behaviour should be done with caution as the mechanism of wetting needs further studies. Also, it is worthwhile mentioning that these measurements were performed 30 days after the laser texturing of the patterns. Also, contaminations such as the absorption of hydrocarbons from

the atmosphere may have influenced the results [53, 49]. However, these preliminary results suggest that the 80 µm and 140 µm grooves may promote a better degree of contact with physiological liquids than the ones with 40 µm grooves. As a matter of fact, directly after fabrication a super hydrophilic behaviour was observed in all the cross-hatched combinations upon cleaning. This was also verified by a contact angle measurement, however, spreading of water on a freshly patterned surface was too rapid and the contact angle too low to collect sufficient number of data points. After cleaning the specimen change in wettability and the super hydrophilicity was lost or even turned to hydrophobicity as in the case of 40 µm groove combinations.

The explanation for losing the super hydrophilic character might be related to several reasons. The nanostructures detected on SEM observations (see Fig.8) increase drastically the overall surface area and the surface free energy but the cleaning peals them off. On the other hand, the oxidation of the surface may also play an important role [54]. Also, photo-induced hydrophilicity (PIH) may be a plausible explanation for this apparent super hydrophilicity [53, 54]. Several authors have reported this behaviour right after laser surface texturing in various types of materials such as coper, titanium and silicon with lasers of different pulse widths [55, 56, 57]. This phenomenon is also referred as photo-functionalisation. In the case of titanium and its alloys, this process is characterised by the TiO_2 photocatalytic activity that upon UV-irradiation leads to formation of radicals and anionic oxygen species which are highly reactive [58, 59, 60]. Thus, the formation of such volatile species will change the chemical stability of the surface and turn it highly reactive [53]. Additionally, some studies have shown that this hydrophilised state can remain for days or even weeks in ambient atmosphere without exposure to cleaning agents [53, 59]. PIH is related to the stoichiometric state of the surface [61]. Rutile hydrophilicity

has been modified with visible light wavelengths by inducing first non-stoichiometry. $TiO_{(2-x)}$ surface can be made photoactive under NIR irritation [61]. Also, Lee *et al.* demonstrated light induced water layer growth on TiO_2 [62] . They describe that the photoadsorbed water layers lead to strong water–water attraction that gives rise to hydrophilicity [62].

3.3. Friction tests

The average dynamic coefficient of friction (COF) shown in Fig.11 on the following page is around 0.4 for all combinations and the static COF values were always higher than the dynamic friction. Grit-blasted surface has a different trend as the final static friction coefficient is slightly smaller than the dynamic coefficient. In the case of Group I combinations, no significant deviation between the initial and final static COF values was observed. Here Group I differs from the other groups. The difference in initial and final COF is the most pronounced in the combinations 20–80 of Group II, and 100–40 and 100–140 of Group III. However, sample orientation may have influenced the results.

Reference measurements were taken with grit-blasted samples and compared against experimental work of performed against bone from the same source. The conditions in this work of Dantas et.al. resemble short-hip-stem implant insertion. Their materials are the same but the grit-basted (R_a = 2.1–2.5 µm) and smooth (R_a =0.3–0.5 µm) Ti−6 Al−4 V surfaces are slightly rougher than presented in this work. Also, the measurement temperature was 17 degrees lower. Despite these differences in measurement parameters the results are in an agreement.

When comparing all the cross-hatched combinations with the grit-blasted re-

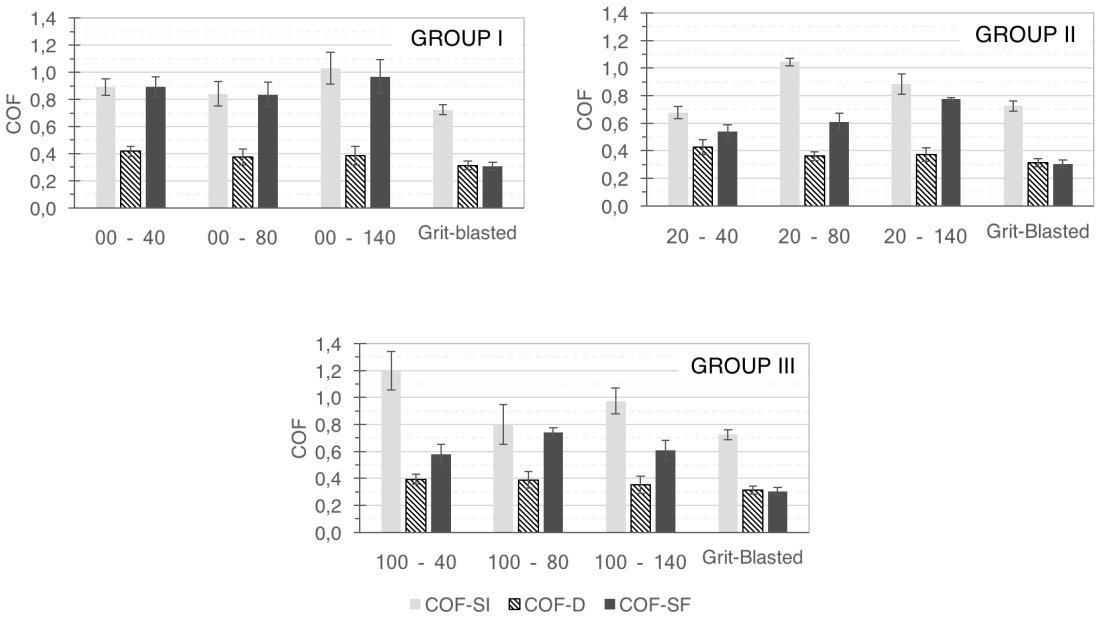

Figure 11: Average coefficients of friction (COF). COF-SI and COF-SF denote the initial and final static coefficient of friction. COF-D stands for dynamic confident of friction. The average dynamic coefficient for all combinations is ∼0.4.

sults, the improvement in friction performance of patterned surfaces is evident. The dynamic coefficient of friction is one tithe grater and the difference in the static counterpart is even higher. Regarding the grit-blasted results, it is noticeable that the final static COF is approximately equal to the dynamic COF. This is interesting as none of the other analysed patterns exhibit this trend. It might indicate that this surface reached a plateau, whereby increasing the sliding distance will not produce significant variations. The explanation for this can be that the measured value is in fact describing the adhesion and compaction of bone against the test-surface. In such case the coefficient of friction is truly not measured between the surface and bone but between compacted bone and bone bulk. Figure 12 presents this so called sliding plane. Thus, this finding indicates that the analysed micropatterns have not

reached this stage in compaction of bone due to their topography and wear of bone is still occurring.

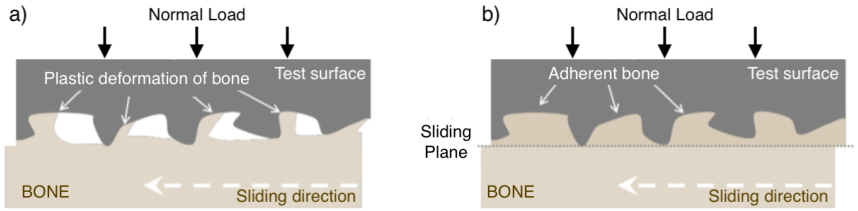

Figure 12: An illustration of adhesion and compaction of bone against a test-surface. a) bone debris amassed between asperities during sliding. b) gliding of the counter body along the sliding plane and compaction of the adhered bone underneath.

460 The morphology of patterned surfaces was observed by SEM in the BSE mode. Bone was found compacting on the samples as expected (see Figures 14, 15 and 16in following subsections). The adhesion and compaction of bone against the test-surface is responsible for the variations in static COF and not the structural integrity of the micropatterns. The grit-blasted surface and pattern 00–40 seem to be the only 465 ones where no surface debris was mixed with bone. Increasing the spacing between grooves did not seem to cause surface features fracturing. Pattern 100–40 after the friction test (Fig.16) has adherent bone compacted and this combination exhibited the highest variation between the initial and final static COF.

470 The grit-blasted surface was also investigated by SEM/EDS. The results were similar to the above-mentioned surfaces with significant amount of compacted bone. Furthermore, this surface did not yield in considerable surface debris. Indeed, when analysing the worn bone surfaces, only some embedded debris was found spread out through the wear tracks. Figure 13 shows the grit-blasted surface with adherent

bone (a) and the wear track left on the bone surface (b) as well as the EDS analysis confirming the transfer of debris form the test-surface (c). This indicates that grit-blasted surfaces may leave debris during the insertion of implant.

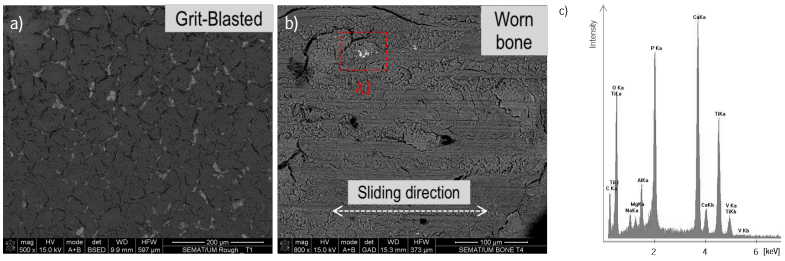

Figure 13: SEM images of (a) worn grit-blasted surface. Darker regions correspond to adhered bone. (b) The respective wear track on bone, where light spots are titanium. (c) The EDS spectrum of A1 confirms the particle as Ti-alloy debris.

Analysis of the surfaces after the friction tests reveals, as expected, that the abraded bone particles seem to allocate on the lower regions of the surfaces such as grooves, pits, groove intersections and in between raised sidewalls. However, in most cases it is possible to observe considerable amount of adhered bone mixed with surface debris. It seems that increasing the groove width leads to a higher fracture whereas increase in spacing between grooves had no effect. It is reasonable to assume that under a load the microcracks open and propagate and indeed the observed microcracks correlate well with the amount of surface debris. In addition, it is worth to mention that despite on the 100–140 combination debris are not visible does not mean that is has higher structural integrity but rather the opposite. In fact, the debris might not have been produced as this combination has showed fracture problems long before the friction tests upon cleaning for example.

In all the three groups, the combinations with 40 µm groove width showed the

smallest content of surface debris mixed with the bone. Explanation for the fracture of structures can be related to the lower mechanical resistance associated with the presence of microcracks. Among the tested surfaces the combinations with 40 µm groove width seemed to be the most advantageous. These surfaces left low wear debris and had higher coefficients of friction significantly than the grit-blasted control surface.

3.3.1. Friction test results – Group I SEM images

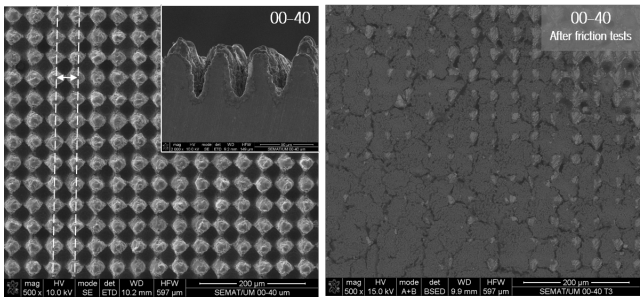

(a) Groove witdth 40 µm

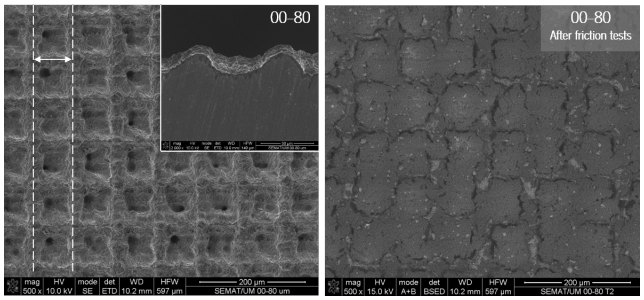

(b) Groove witdth 80 µm

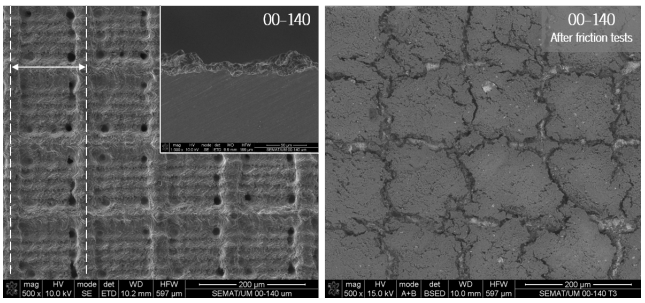

(c) Groove witdth 140 µm

Figure 14: SEM images of the tested combinations from Group I against bovine bone. SE-images (left) show the topographies before test and the insets magnify the microgrooves. The BSE images of the worn surfaces (right) visualise the transferred bone, darker regions correspond to bone.

3.3.2. Friction test results – Group II SEM images

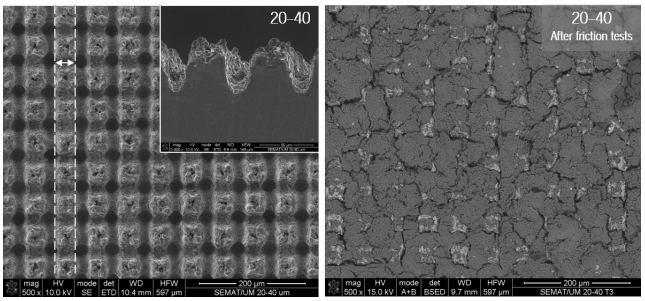

(a) Groove witdth 40 µm

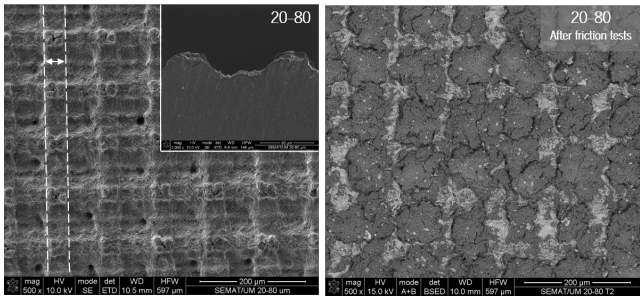

(b) Groove witdth 80 µm

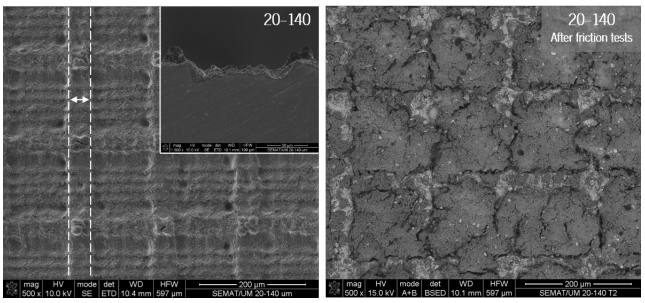

(c) Groove witdth 140 µm

Figure 15: SEM images of the tested combinations from Group II against bovine bone. Secondary electron images (left) show the topographies before friction test. In the BSE images of corresponding worn surfaces (right) the darker regions correspond to transferred bone. The scale bar for SE and BSE images is 200 µm and 50 µm for the insets.

3.3.3. Friction test results – Group III SEM images

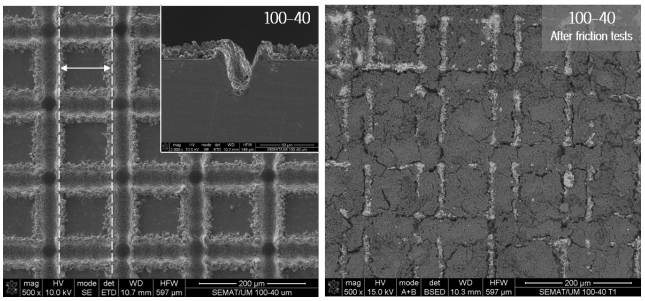

(a) Groove witdth 40 µm

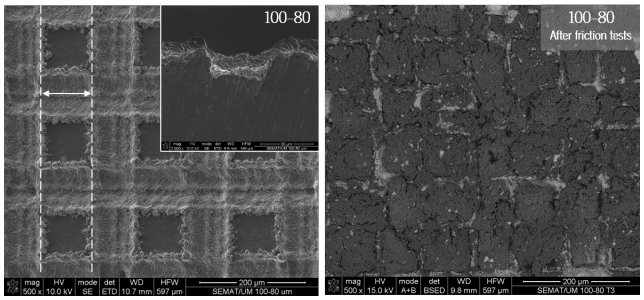

(b) Groove witdth 80 µm

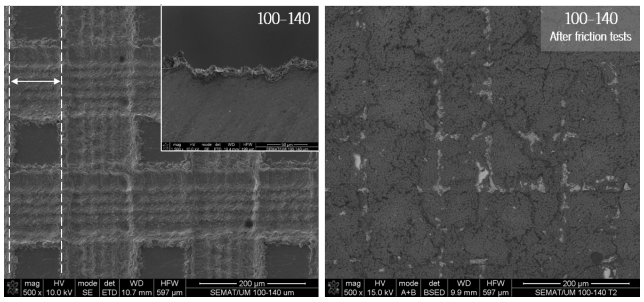

(c) Groove witdth 140 µm

Figure 16: SEM images of the tested combinations from Group III against bovine bone. Secondary electron images (left) before friction test and In the BSE images of the corresponding worn surfaces (right) the darker regions correspond to transferred bone. The scale bar for SE and BSE images is 200 µm and 50 µm for the insets.

4. Discussion

The topographical measurements of the produced cross-hatched combinations showed a good agreement between the designed and obtained features. Increasing groove width leads to decrease in the density of features, the groove shape changes from U-shaped to squared and the features get less pronounced. Furthermore, the evolution of the distinct feature follows a similar tendency in all of the groups. Regarding the depth of the grooves, as expected increasing the groove width resulted in smaller groove depths. Thus, the combinations with higher groove width and spacing were the shallowest ones ($\sim 15.2\,\mu m$) and the micropatterns with narrower grooves had the higher groove depths (between 32.3 µm and 49 µm). Moreover, the roughness results followed the same trend in which the average roughness values were higher on the combinations with lower or without spacing and narrower grooves ($R_a \sim 5$–$6\,\mu m$). As expected, increasing the groove width decreased the average roughness of the surface.

The wetting behaviour studied by a sessile drop method showed that combinations with groove width of 40 µm were hydrophobic ($\theta' \sim 120°$), whereas the combinations with wider grooves possessed a hydrophilic behaviour with average contact angles similar to values recorded for a control smooth surface. The spacing between grooves did not seem to affect the wettability. Further observations suggested that 40 µm groove combinations may be in a metastable Cassie-Baxter state where air is imprisoned underneath the droplet between topographical discontinuities. On the other hand, the 80 µm and 140 µm groove combinations may promote Wenzel model wetting where the surface is completely or nearly totally wetted by the testing liquids. No significant difference in the trend of spreading was observed between UPW

and glycerol. Prior cleaning all the textured surfaces were superhydrophilic but upon cleaning and drying this wetting behaviour changed. Preserving the superhydrophilic character could promote antibacterial response [34]. Further, modulating the observed change into less hydrophobic in the case of patterns with 40 µm groove width could benefit osseointegration.

From the friction tests it was found that variations in the static coefficient of friction are not associated with the structural integrity of the micropatterns but with the mechanism of adhesion and compaction of bone against the test surface. Regarding the structural integrity of the produced surfaces, it was found that if microcracks were present on the surface they led to some fatigue problems and fracture of the features. The debris may result in premature failure of the implants by promoting metal sensitivity and osteolysis. When comparing the performance of these micropatterns with a grit-blasted surface, the combinations with groove width of 40 µm seemed to be the most advantageous. These surfaces were characterised by leaving low wear debris and having the coefficients of friction significantly higher than recorded for the grit-blasted surface. These properties suggest a possible improvement in the implant stability after insertion.

5. Conclusions

The main purpose of the work was to develop novel textures onto Ti−6 Al−4 V surfaces in order to improve the overall stability and osseointegration process of dental implants. Limitations of the study prevent declaring tissue response of the presented micropatterns. This work succeeded in laser surface texturing of nine cross-hatch micropatterns on biomedical grade titanium alloy with good reproducibility. The structural integrity of the features is good with only a few defects. The obtained

micropatterns vary in wetting and friction against bone and the characteristics originate from different texturing plans with the same operation parameters. The macro scale wetting may be adjustable by patterning and the surfaces generally have higher coefficients of friction than the grit-blasted control samples. The optimisation of LST patterns gives rise to new designs for mechanically stable implant-bone connection and functional surfaces. After all, there is still potential to reduce healing times and achieve long-lasting osseointegration.

Conflict of interest

The authors report no conflicts of interest.

Acknowledgements

This work has been supported by FCT(Fundação para a Ciência e Tecnologia – Portugal) in the scope of the projects UID/ EEA/ 04436/ 2013 and NORTE-01-0145-FEDER-000018-HAMaBICo. The contact angle measurements were performed with technician Marta Teixeira at the Textile Department on University of Minho.

References

[1] P. Bouchard, J. Malet, F. Mora, Implant Dentistry at a Glance, Wiley-Blackwell, 2012.

[2] S. Sakka, K. Baroudi, M. Z. Nassani, Factors associated with early and late failure of dental implants, Journal of investigative and clinical dentistry 3 (4)

(2012) 258–261. doi:https://doi.org/10.1111/j.2041-1626.2012.00162.x.

[3] J. A. Porter, et al., Success or failure of dental implants? a literature review with treatment considerations., General dentistry 53 (6) (2005) 423–32.

[4] H. Mohajerani, R. Roozbayani, S. Taherian, R. Tabrizi, The risk factors in early failure of dental implants: a retrospective study, Journal of Dentistry 18 (4) (2017) 298.

[5] M. Gasik, Understanding biomaterial-tissue interface quality: combined in vitro evaluation, Science and Technology of advanced MaTerialS 18 (1) (2017) 550–562.

[6] L. Rimondini, M. Gasik, Bacterial attachment and biofilm formation on biomaterials: The case of dental and orthopaedic implants, in: Biomaterials and Immune Response, CRC Press, 2018, pp. 87–120.

[7] G. Byrne, Fundamentals of implant dentistry, John Wiley & Sons, 2014.

[8] A. M. Ballo, O. Omar, W. Xia, A. Palmquist, Dental implant surfaces–physicochemical properties, biological performance, and trends, in: Implant Dentistry-A Rapidly Evolving Practice, InTech, 2011. doi:https://doi.org/10.5772/17512.

[9] K. Turzo, Surface aspects of titanium dental implants, in: Biotechnology-Molecular Studies and Novel Applications for Improved Quality of Human Life, InTech, 2012, pp. 135–158. doi:https://doi.org/10.5772/29288.

[10] L. Feller, Y. Jadwat, R. A. Khammissa, R. Meyerov, I. Schechter, J. Lemmer, Cellular responses evoked by different surface characteristics of intraosseous titanium implants, BioMed research international 2015. doi:http://dx.doi.org/10.1155/2015/171945.

[11] D. Noorthoek, Macroscopic and microscopic dental implant design: a review of the literature, University of Florida.

[12] N. Meredith, A review of implant design, geometry and placement, Appl Osseointgrated Res 6 (2008) 6–12.

[13] V. A. O. Toledo, Dental implant surface modifications and osteointegration, Ph.D. thesis, Universidade Católica Portuguesa (2013).

[14] S. Faegh, Mechanism of load transfer along bone-dental implant, Ph.D. thesis, Northeastern University (2009).

[15] K. Prasad, O. Bazaka, M. Chua, M. Rochford, L. Fedrick, J. Spoor, R. Symes, M. Tieppo, C. Collins, A. Cao, et al., Metallic biomaterials: Current challenges and opportunities, Materials 10 (8) (2017) 884.

[16] M. Bidez, C. Misch, Force transfer in implant dentistry: basic concepts and principles., The Journal of oral implantology 18 (3) (1992) 264–274.

[17] R. Osman, M. Swain, A critical review of dental implant materials with an emphasis on titanium versus zirconia, Materials 8 (3) (2015) 932–958.

[18] D. Brunette, P. Tengvall, M. Textor, P. Thomsen, Titanium in medicine: material science, surface science, engineering, biological responses and medical applications (engineering materials) (2001).

[19] M. Kulkarni, A. Mazare, P. Schmuki, A. Iglič, Biomaterial surface modification of titanium and titanium alloys for medical applications, Nanomedicine 111 (2014) 111.

[20] X. Liu, P. K. Chu, C. Ding, Surface modification of titanium, titanium alloys, and related materials for biomedical applications, Materials Science and Engineering: R: Reports 47 (3-4) (2004) 49–121. doi:https://doi.org/10.1016/j.mser.2004.11.001.

[21] B. Yang, M. Uchida, H.-M. Kim, X. Zhang, T. Kokubo, Preparation of bioactive titanium metal via anodic oxidation treatment, Biomaterials 25 (6) (2004) 1003–1010.

[22] M. Gasik, L. Van Mellaert, D. Pierron, A. Braem, D. Hofmans, E. De Waelheyns, J. Anné, M.-F. Harmand, J. Vleugels, Reduction of biofilm infection risks and promotion of osteointegration for optimized surfaces of titanium implants, Advanced healthcare materials 1 (1) (2012) 117–127. doi:https://doi.org/10.1002/adhm.201100006.

[23] M. Gasik, A. Braem, A. Chaudhari, J. Duyck, J. Vleugels, Titanium implants with modified surfaces: Meta-analysis of in vivo osteointegration, Materials Science and Engineering: C 49 (2015) 152–158. doi:https://doi.org/10.1016/j.msec.2014.12.074.

[24] J. Rosales-Leal, M. Rodríguez-Valverde, G. Mazzaglia, P. Ramón-Torregrosa, L. Diaz-Rodriguez, O. Garcia-Martinez, M. Vallecillo-Capilla, C. Ruiz, M. Cabrerizo-Vílchez, Effect of roughness, wettability and morphology of engineered titanium surfaces on osteoblast-like cell adhesion, Colloids and Sur-

faces A: Physicochemical and Engineering Aspects 365 (1-3) (2010) 222–229. doi:https://doi.org/10.1016/j.colsurfa.2009.12.017.

[25] V. D. Rani, L. Vinoth-Kumar, V. Anitha, K. Manzoor, M. Deepthy, V. N. Shantikumar, Osteointegration of titanium implant is sensitive to specific nanostructure morphology, Acta biomaterialia 8 (5) (2012) 1976–1989. doi:https://doi.org/10.1016/j.actbio.2012.01.021.

[26] A. Wennerberg, T. Albrektsson, Effects of titanium surface topography on bone integration: a systematic review, Clinical oral implants research 20 (s4) (2009) 172–184. doi:https://doi.org/10.1111/j.1600-0501.2009.01775.x.

[27] B. S. Kopf, S. Ruch, S. Berner, N. D. Spencer, K. Maniura-Weber, The role of nanostructures and hydrophilicity in osseointegration: In-vitro protein-adsorption and blood-interaction studies, Journal of biomedical materials research Part A 103 (8) (2015) 2661–2672. doi:https://doi.org/10.1002/jbm.a.35401.

[28] A. T. Nguyen, S. R. Sathe, E. K. Yim, From nano to micro: topographical scale and its impact on cell adhesion, morphology and contact guidance, Journal of Physics: Condensed Matter 28 (18) (2016) 183001. doi:https://doi.org/10.1088/0953-8984/28/18/183001.

[29] R. A. Gittens, R. Olivares-Navarrete, A. Cheng, D. M. Anderson, T. McLachlan, I. Stephan, J. Geis-Gerstorfer, K. H. Sandhage, A. G. Fedorov, F. Rupp, et al., The roles of titanium surface micro/nanotopography and wettability on the differential response of human osteoblast lineage cells, Acta biomaterialia 9 (4) (2013) 6268–6277. doi:https://doi.org/10.1016/j.actbio.2012.12.002.

[30] J. Ballester-Beltrán, M. J. Biggs, M. J. Dalby, M. Salmerón-Sánchez, A. Leal-Egaña, Sensing the difference: the influence of anisotropic cues on cell behavior, Frontiers in Materials 2 (2015) 39. doi:https://doi.org/10.3389/fmats.2015.00039.

[31] P. Maressa, L. Anodio, A. Bernasconi, A. G. Demir, B. Previtali, Effect of surface texture on the adhesion performance of laser treated ti6al4v alloy, The journal of adhesion 91 (7) (2015) 518–537. doi:https://doi.org/10.1080/00218464.2014.933809.

[32] Y. Liu, X. Zhang, P. Hao, The effect of topography and wettability of biomaterials on platelet adhesion, Journal of adhesion science and Technology 30 (8) (2016) 878–893. doi:https://doi.org/10.1080/01694243.2015.1129883.

[33] K. Anselme, L. Ploux, A. Ponche, Cell/material interfaces: influence of surface chemistry and surface topography on cell adhesion, Journal of Adhesion Science and Technology 24 (5) (2010) 831–852. doi:https://doi.org/10.1163/016942409X12598231568186.

[34] C. M. Bhadra, V. K. Truong, V. T. Pham, M. Al Kobaisi, G. Seniutinas, J. Y. Wang, S. Juodkazis, R. J. Crawford, E. P. Ivanova, Antibacterial titanium nano-patterned arrays inspired by dragonfly wings, Scientific reports 5 (2015) 16817.

[35] K. Kuroda, M. Okido, Osteoconductivity of protein adsorbed titanium implants using hydrothermal treatment, in: Materials Science Forum, Vol. 879, Trans Tech Publ, 2017, pp. 1049–1052.

[36] J. Wei, T. Igarashi, N. Okumori, T. Igarashi, T. Maetani, B. Liu, M. Yoshinari, Influence of surface wettability on competitive protein adsorption and initial

attachment of osteoblasts, Biomedical Materials 4 (4) (2009) 045002. doi:https://doi.org/10.1088/1748-6041/4/4/045002.

[37] L. Hao, H. Yang, C. Du, X. Fu, N. Zhao, S. Xu, F. Cui, C. Mao, Y. Wang, Directing the fate of human and mouse mesenchymal stem cells by hydroxyl–methyl mixed self-assembled monolayers with varying wettability, Journal of Materials Chemistry B 2 (30) (2014) 4794–4801. doi:https://doi.org/10.1039/C4TB00597J.

[38] R. A. Gittens, L. Scheideler, F. Rupp, S. L. Hyzy, J. Geis-Gerstorfer, Z. Schwartz, B. D. Boyan, A review on the wettability of dental implant surfaces ii: biological and clinical aspects, Acta biomaterialia 10 (7) (2014) 2907–2918. doi:https://doi.org/10.1016/j.actbio.2014.03.032.

[39] W. Perrin, W. Tarn, Handbook of Metal Etchants, CRC Press Boca Raton, Florida United States of America, 1991.

[40] L. Diogenes, Laser surface texturing-their applications, Tech. rep., SAE Technical Paper (2012). doi:https://doi.org/10.4271/2012-36-0332.

[41] J. D. Majumdar, I. Manna, Laser-assisted fabrication of materials, Vol. 161, Springer Science & Business Media, 2012.

[42] ISO 11146-2:2005(en), Lasers and laser-related equipment – Test methods for laser beam widths, divergence angles and beam propagation ratios., International Organization for Standardization, Geneva, Switzerland.
URL https://www.iso.org/obp/ui/#iso:std:iso:11146:-1:ed-1:v1:en

[43] B. J. Griffiths, Manufacturing surface technology: Surface integrity & functional performance (2001).

[44] ISO 4288:1996(en), Geometrical Product Specifications (GPS) – Surface texture: Profile method – Rules and procedures for the assessment of surface texture., International Organization for Standardization, Geneva, Switzerland.
URL https://www.iso.org/obp/ui/#iso:std:iso:4288:ed-2:v1:en

[45] M. Bussoli, T. Desai, D. Batani, B. Gakovic, M. Trtica, Nd: Yag laser interaction with titanium implant surfaces for medical applications, Radiation Effects & Defects in Solids 163 (4-6) (2008) 349–356. doi:https://doi.org/10.1080/10420150701777678.

[46] L. Lavisse, D. Grevey, C. Langlade, B. Vannes, The early stage of the laser-induced oxidation of titanium substrates, Applied Surface Science 186 (1-4) (2002) 150–155. doi:https://doi.org/10.1016/S0169-4332(01)00761-9.

[47] L. Yue, Z. Wang, L. Li, Material morphological characteristics in laser ablation of alpha case from titanium alloy, Applied Surface Science 258 (20) (2012) 8065–8071. doi:https://doi.org/10.1016/j.apsusc.2012.04.173.

[48] R. Le Harzic, N. Huot, E. Audouard, C. Jonin, P. Laporte, S. Valette, A. Fraczkiewicz, R. Fortunier, Comparison of heat-affected zones due to nanosecond and femtosecond laser pulses using transmission electronic microscopy, Applied Physics Letters 80 (21) (2002) 3886–3888. doi:https://doi.org/10.1063/1.1481195.

[49] M. Annamalai, K. Gopinadhan, S. A. Han, S. Saha, H. J. Park, E. B. Cho, B. Kumar, A. Patra, S.-W. Kim, T. Venkatesan, Surface energy and wettability of van der waals structures, Nanoscale 8 (10) (2016) 5764–5770. doi:https://doi.org/10.1039/C5NR06705G.

[50] C. Langlade, A. Vannes, J. Krafft, J. Martin, Surface modification and tribological behaviour of titanium and titanium alloys after yag-laser treatments, Surface and Coatings Technology 100 (1998) 383–387. doi:https://doi.org/10.1016/S0257-8972(97)00653-1.

[51] A. P. Del Pino, P. Serra, J. Morenza, Oxidation of titanium through nd: Yag laser irradiation, Applied surface science 197 (2002) 887–890. doi:https://doi.org/10.1016/S0169-4332(02)00447-6.

[52] A. Fasasi, S. Mwenifumbo, N. Rahbar, J. Chen, M. Li, A. Beye, C. Arnold, W. Soboyejo, Nano-second uv laser processed micro-grooves on ti6al4v for biomedical applications, Materials Science and Engineering: C 29 (1) (2009) 5–13. doi:https://doi.org/10.1016/j.msec.2008.05.002.

[53] R. Yamauchi, T. Itabashi, K. Wada, T. Tanaka, G. Kumagai, Y. Ishibashi, Photofunctionalised ti6al4v implants enhance early phase osseointegration, Bone and Joint Research 6 (5) (2017) 331–336. doi:https://doi.org/10.1302/2046-3758.65.BJR-2016-0221.R1.

[54] S. Khan, G. Azimi, B. Yildiz, K. K. Varanasi, Role of surface oxygen-to-metal ratio on the wettability of rare-earth oxides, Applied Physics Letters 106 (6) (2015) 061601. doi:https://doi.org/10.1063/1.4907756.

[55] D. V. Ta, A. Dunn, T. J. Wasley, R. W. Kay, J. Stringer, P. J. Smith, C. Connaughton, J. D. Shephard, Nanosecond laser textured superhydrophobic metallic surfaces and their chemical sensing applications, Applied Surface Science 357 (2015) 248–254. doi:https://doi.org/10.1016/j.apsusc.2015.09.027.

[56] S.-F. Tseng, W.-T. Hsiao, M.-F. Chen, K.-C. Huang, S.-Y. Hsiao, Y.-S. Lin,

C.-P. Chou, Surface wettability of silicon substrates enhanced by laser ablation, Applied Physics A 101 (2) (2010) 303–308. doi:10.1007/s00339-010-5821-y. URL https://doi.org/10.1007/s00339-010-5821-y

[57] A. Cunha, A. P. Serro, V. Oliveira, A. Almeida, R. Vilar, M.-C. Durrieu, Wetting behaviour of femtosecond laser textured Ti−6 Al−4 V surfaces, Applied surface science 265 (2013) 688–696. doi:https://doi.org/10.1016/j.apsusc.2012.11.085.

[58] M. S. Al Qahtani, Y. Wu, S. Spintzyk, P. Krieg, A. Killinger, E. Schweizer, I. Stephan, L. Scheideler, J. Geis-Gerstorfer, F. Rupp, Uv-a and uv-c light induced hydrophilization of dental implants, Dental Materials 31 (8) (2015) e157–e167. doi:https://doi.org/10.1016/j.dental.2015.04.011.

[59] F. Rupp, M. Haupt, H. Klostermann, H.-S. Kim, M. Eichler, A. Peetsch, L. Scheideler, C. Doering, C. Oehr, H. Wendel, et al., Multifunctional nature of uv-irradiated nanocrystalline anatase thin films for biomedical applications, Acta biomaterialia 6 (12) (2010) 4566–4577. doi:https://doi.org/10.1016/j.actbio.2010.06.021.

[60] X.-L. Zhou, X.-Y. Zhu, J. White, Photochemistry at adsorbate/metal interfaces, Surface science reports 13 (3-6) (1991) 73–220.

[61] S. B. Rosenthal, Changing the wetting properties of titanium dioxide surfaces with visible and near infrared light, Ph.D. thesis, Johns Hopkins University (2016).

[62] K. Lee, Q. Kim, S. An, J. An, J. Kim, B. Kim, W. Jhe, Superwetting of TiO_2 by

light-induced water-layer growth via delocalized surface electrons, Proceedings of the National Academy of Sciences (2014) 201319001.

Annex

I - XPS data and curve fitting

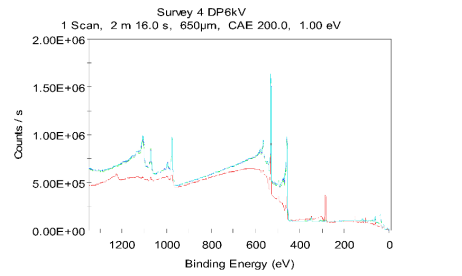

Polished

Ref.	Name	Peak BE	Height CPS	Height Ratio	Area CPS.eV	Area Ratio	FWHM fit param (eV)
C	Ti2p3 met	454,53	2855,91	0,07	6515,38	0,09	2,15
D	Ti2p3 TiOx	457,66	19323,66	0,5	48806,47	0,67	2,21
E	Ti2p3 TiO2	459,37	38838,15	1	72403,29	1	1,44
F	Ti2p 4 D	464,41	12870,18	0,33	42875,04	0,59	3,15

Peak Table :	Polished	
Name	Peak BE	Atomic %
Al2p met	71,9	0,43
Al2p AlOx	74,59	4,69
Ti2p3 met	**454,53**	**1,52**
Ti2p3 TiOx	457,66	11,39
Ti2p3 TiO2	459,37	16,9
Ti2p 4 D	464,41	0
V2p 4 A	513,21	0,13
V2p 4 C	522,87	0,19
V2p 4 D	515,86	0,3
O1s	530,88	58,41
C1s	285,73	6,05

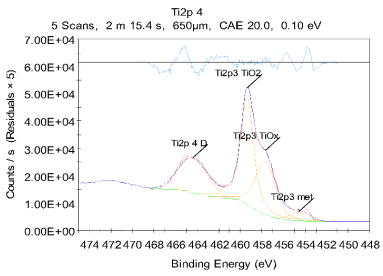

Figure 17: XPS results. Polished sample.

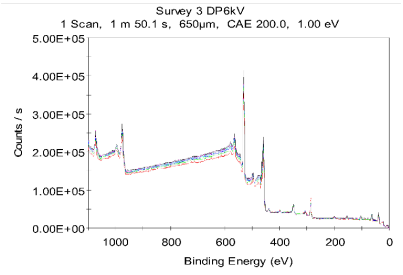

00-40

Ref.	Name	Peak BE	Height CPS	Height Ratio	Area CPS.eV	Area Ratio	FWHM fit param (eV)
B	Ti2p3 met	455,57	644,12	0,05	2411,27	0,11	3,22
C	Ti2p3 TiOx	457,84	1996,28	0,16	3556,71	0,16	1,66
D	Ti2p3 TiO2	459,37	12877,85	1	21696,82	1	1,33
E	Ti2p 4 D	464,88	3656,83	0,28	10167,81	0,47	2,57

Peak Table :	00-40	
Name	Peak BE	Atomic %
Al2p met	71,9	1,52
Al2p AlOx	74,72	2,4
Ti2p3 met	**455,57**	**2**
Ti2p3 TiOx	457,84	2,95
Ti2p3 TiO2	459,37	18,02
Ti2p 4 D	464,88	0
V2p3 metal	513,31	0,07
V2p3 VOx	523,1	0,22
V2p 4 D	516,4	0
O1s met	531,04	33,52
O1s C-O	532,26	18,26
C1s 1 A	285,5	8,82
C1s 1 B	286,52	10,59
C1s 1 C	289,76	1,64

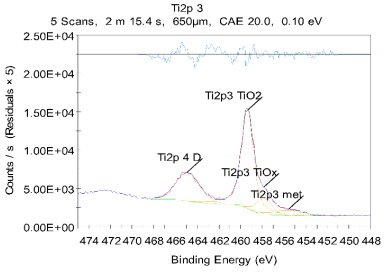

Figure 18: XPS results. Pattern 00–40. Group I, Groove width 40 µm.

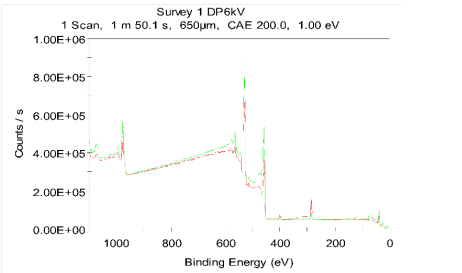

20-80

Ref.	Name	Peak BE	Height CPS	Height Ratio	Area CPS.eV	Area Ratio	FWHM fit param (eV)
D	Ti2p3 met	454,89	1189,87	0,04	2382,25	0,05	1,88
E	Ti2p3 TiOx	457,77	5479,76	0,19	13133,69	0,26	2,28
F	Ti2p3 TiO2	459,2	28819,59	1	51374,46	1	1,38
G	Ti2p 4 D	464,66	8613,85	0,3	24235,22	0,47	2,66

Peak Table : 20-80

Name	Peak BE	Atomic %
C1s C-C	285,15	6,23
C1s C=O	289,41	1,06
C1s C-O	286,53	2,7
Ti2p3 met	**454,89**	**0,83**
Ti2p3 TiOx	457,77	4,61
Ti2p3 TiO2	459,2	18,03
Ti2p 4 D	464,66	0
V2p3 metal	513,17	0,05
V2p3 VOx	523,54	0,2
V2p 4 D	516,08	0,49
C1s	285,22	10,09
O1s met	530,76	34,36
O1s C-O	531,71	15,43
Al2p met	71,9	0,64
Al2p AlOx	74,55	5,27

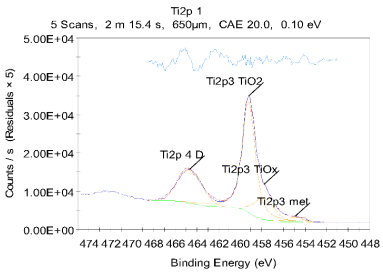

Figure 19: XPS results. Pattern 20–80. Group II, Groove width 80 µm.

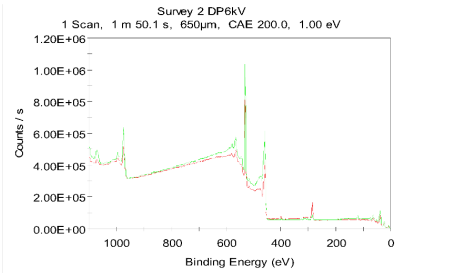

100-80

Ref.	Name	Peak BE	Height CPS	Height Ratio	Area CPS.eV	Area Ratio	FWHM fit param (eV)
B	Ti2p3 met	454,47	946,53	0,03	1813,57	0,03	1,8
C	Ti2p3 TiOx	457,94	8299,58	0,27	22942,48	0,43	2,43
D	Ti2p3 TiO2	459,26	30705,34	1	53271,4	1	1,34
E	Ti2p 4 D	464,66	9936,05	0,32	28785,49	0,54	2,73

Peak Table 100-80

Name	Peak BE	Atomic %
Al2p met	71,9	0,64
Al2p AlOx	74,57	5,38
Ti2p3 met	**454,47**	**0,63**
Ti2p3 TiOx	457,94	7,97
Ti2p3 TiO2	459,26	18,52
Ti2p 4 D	464,66	0
V2p3 meta	513,04	0,12
V2p3 VOx	523,46	0,34
V2p 4 D	516,1	0
O1s met	530,79	37,91
O1s C-O	531,58	18,82
C1s 1 A	285,12	4,7
C1s 1 B	286,14	3,82
C1s 1 C	289,31	1,17

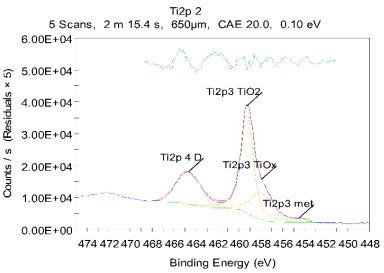

Figure 20: XPS results. Pattern 100–80. Group III, Groove width 80 µm.